Numerical characterization of micro heat exchangers using experimentally tested porous aluminum layers

B. V. Antohe and J. L. Lage
Mechanical Engineering Department, Southern Methodist University, Dallas, Texas

D. C. Price and R. M. Weber
Defense Systems & Electronics Group, Texas Instruments, Plano, Texas

A microporous heat exchanger device is being developed for cooling high-power electronics. The device uses a mechanically compressed aluminum porous layer to improve the heat transfer at the coolant/solid interface and to provide more uniform cooling of the electronics. The hydraulic characteristics (porosity, permeability, and Forchheimer coefficient) of nine distinct compressed layers are obtained experimentally. These layers have porosity from 0.3 to 0.7 and permeability from 1.8×10^{-10} m^2 to 1.2×10^{-9} m^2. The inertia coefficient varies from 0.3 to 0.9. These hydraulic characteristics are used in the numerical simulations of a real microporous heat exchanger for cooling phased-array radars in development. Thermal and hydraulic performances are illustrated in terms of total pressure drop across the heat exchanger, maximum temperature difference in the direction transverse to the electronic modules, and maximum temperature within the coolant passage. Results indicate that the proposed design is capable of achieving a maximum transverse temperature difference of 2°C using polyalphaolephin as coolant.

Keywords: cooling of electronics; microporous heat exchangers; porous media

Introduction

The development of advanced high-frequency microwave systems faces very challenging cooling restrictions in terms of flow rate and temperature of the delivered coolant. Precise control of the phase of each signal from each microwave module is critical to achieving the required overall system performance.

From a system operational view, it is highly desirable that the electrical performance of identical components in each module have identical electrical characteristics. One major means to do this is to have the operating temperatures of identical parts the same. Therefore, minimizing temperature gradients between identical components in each housing module is a fundamental requirement. To provide reliable operation, it is necessary to have the operating temperatures as low as possible, within certain bounds. This is achieved by improving the heat transfer coefficient of the cold plate aperture, thereby reducing the temperature rise from the fluid to cold plate mounting surface. This reduction lowers the device junction temperature and significantly improves the array reliability.

A conventional microwave aperture uses cold plates (heat exchangers) with modules mounted as shown in Figure 1. When the coolant circulates through the internal passageways of the cold plate, the heat dissipated by each module is transferred to the flowing coolant and transported away from the array. A series-flow arrangement (Figure 1A) results in a large temperature difference between identical components in successive modules since the temperature of the cooling fluid increases along its travel path. Shown in the lower part of Figure 1A is a typical resulting temperature gradient along a cross section of the array, which is undesirable. The previous solution to this problem requires sophisticated, computerized calibration techniques to compensate for the differences in electrical characteristics of each component caused by each module operating at a different temperature.

A parallel-flow arrangement (Figure 1B), if attainable, would result in a uniform temperature across the modules and optimum array electrical performance. For most high-frequency microwave arrays, however, the scale of the array is small, and prior attempts to utilize parallel-flow cold plates have been unsuccessful, because the changes in flow direction required by the small scale and the lack of adequate plenum space result in poorly distributed coolant flow. This poorly distributed flow causes excessive temperature differences between modules, the very problem that the parallel-flow concept was intended to solve.

Address reprint requests to Prof. J. L. Lage, Mechanical Engineering Dept., SMU, Dallas, TX 75275-0337, USA.

Received 9 February 1996; accepted 26 June 1996

Int. J. Heat and Fluid Flow 17: 594–603, 1996

655 Avenue of the Americas, New York, NY 10010

0142-727X/96/$15.00
PII S0142-727X(96)00085-6

To obtain a parallel-flow arrangement with a flow uniformity not obtained previously, a new approach to the design of a cold plate is necessary. The new cold-plate design, considered in the present effort, consists of inserting a porous metallic layer inside the cold-plate aperture (Figure 1B). Porous medium, a solid structure with several interconnected small channels, is known for its ability to equalize fluid flow pressure. By placing a porous layer within the cold-plate aperture, the pressure gradient (along the modules) from inlet to outlet plena is equalized, resulting in a parallel-flow, thereby maintaining the temperature of the components—and by consequence their electrical characteristics—substantially the same.

We mention in passing that the microporous cold plate concept considered here is related to heat exchangers designed with mesh and brush inserts (Bergles 1985), modern microchannel heat exchanger (Walpole and Missaggia 1993) and microsintered heat exchangers (Lindemuth et al. 1994). All these devices attempt to improve the weak heat transfer at the fluid side of solid-fluid heat exchangers by increasing the solid-fluid interface area (fin effect) and by inducing fluid mixing (turbulence and dispersion effects). Previous studies with metal wool filled copper tubes (Kuzay et al. 1991), flat-plate rectangular microchannels (Peng et al. 1995), and sintered heat sinks (Lindemuth et al.) support our expectations that a microporous cold plate can exhibit exceptional thermal performance.

The main advantages of the microporous design, as compared with metal wool filling, microchannels, and microsintering techniques, are: (1) much broader physical characterization (e.g., porosity range from 30 to 90%); (2) precise specification (good repeatability); (3) superior manufacturing characteristics (brazing); and (4) structural rigidity.

The material considered for the microporous inserts, aluminum alloy 6101-T6 porous matrix, has been carefully chosen. It has low density for small-to-negligible impact on the total weight of the system, intrinsic mechanical strength for structural rigidity, and good material compatibility for brazing the porous layer with the interior surfaces of the cold plate. In addition, the thermal conductivity of this porous material is much higher than that of the coolants used in electronics. Therefore, the effective thermal conductivity of the saturated porous region is much higher than the thermal conductivity of the fluid.

The rate of fluid flow through the cold plate is determined by the form of the fluid (coolant) flow passage. The pressure drop across the porous layer, for a given flow rate and fluid dynamic viscosity, depends on the structure of the medium characterized by its porosity, permeability, and inertia (or Forchheimer) coefficient. These properties of the metallic microporous layers must be obtained experimentally, because predictive models for this type of porous layers do not exist. In what follows, we report results of numerical simulations of microporous cold plates using hydraulic parameters of mechanically compressed porous aluminum layers obtained experimentally.

Theoretical model

Consider the flow of incompressible Newtonian fluid with constant properties through a heterogeneous system (Figure 1C). The fluid saturates the rigid, homogeneous, and isotropic porous matrix. Fluid and solid matrix are supposed to be in thermal equilibrium. The vertical (z) variation of pressure can be neglected in a slender enclosure, $h \ll (t, d)$. The velocity field is

Notation

C	average pore size, Equation 13
c_F	Forchheimer coefficient
c_p	specific heat, J/kgK
d	enclosure depth, m
e	inlet and outlet enclosure depth, m
h	enclosure thickness, m
H	experimental porous layer thickness, m
J	effective viscosity coefficient
k	thermal conductivity, W/m^{2}K
K	permeability, m^2
k_B	constant
Kn	Knudsen number, Equation 11
L	experimental porous layer length, m
p	pressure, Pa
q	heat, W
$\dot{Q}$	volumetric flow rate, m^3/s
r	compression ratio
R_m	radius of collision cross section, m
S	cross-section area, m^2
s	shape function, Equation 1
t	enclosure width, m
T	temperature, K
U	uncertainty
V	volume
$\mathbf{V}$	two-dimensional velocity vector
v_D	Darcy velocity of experimental tests, m/s
W	experimental porous layer width, m
u, v, w	Cartesian fluid (seepage) velocity components, m/s
x, y, z	Cartesian coordinates, m

Greek

β	auxiliary parameter
Δ	difference
ϕ	porosity
Γ	auxiliary parameter
λ	mean path of gas molecules, Equation 12, m
μ	dynamic viscosity, kg/sm
ν	kinematic viscosity, m^2/s
ρ	density, kg/m^3

Superscripts

$(\ )'$	porous volume averaged
$(\ )''$	per unit of area
$(\ )'''$	per unit of volume
$\overline{(\ )}$	surface averaged

Subscripts

b	bottom
c	compressed microporous layer
f	fluid
h	heating
in	inlet
m	fluid and solid matrix
max	maximum
min	minimum
out	outlet
s	solid
t	top
u	uncompressed porous matrix

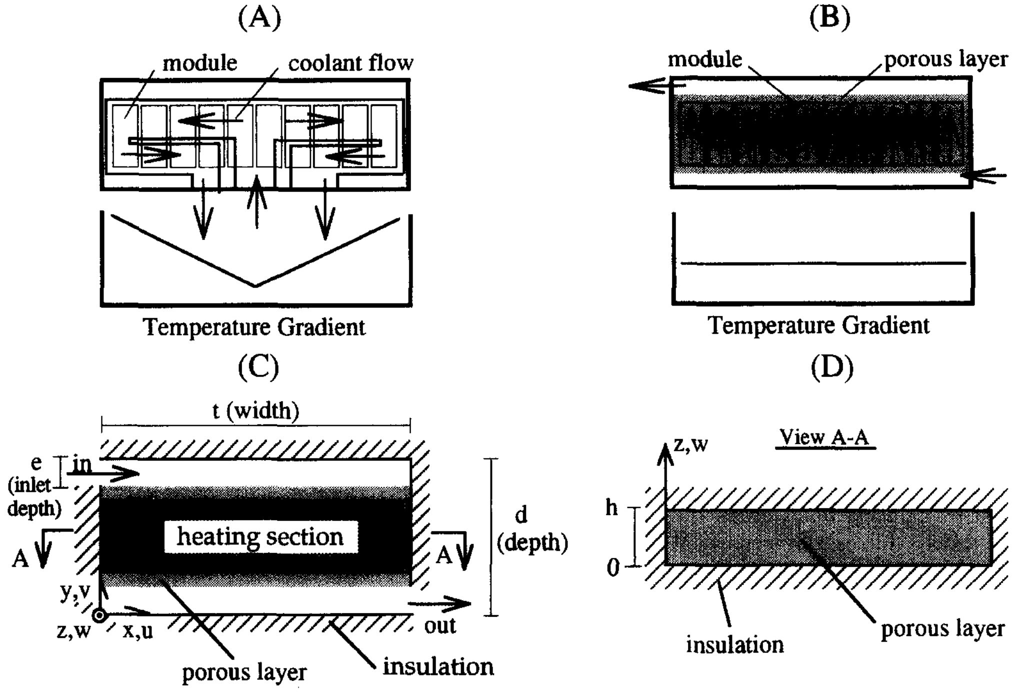

Figure 1 Phased-array radar electronic slat: temperature gradient across modules with in series flow configuration (A) or parallel flow configuration (B); model representation of the physical system (C) with porous layer sandwiched between aluminum plates (D)

then assumed to be fully developed in z within both nonporous and porous regions. The three-dimensional (3-D) velocity components can be written as the product of the z-averaged horizontal velocity components u and v with a shape function $s(z)$ that determines the velocity profile in the z-direction,

$$u(x,y,z) = u(x,y)s_{f,m}(z), \quad v(x,y,z) = v(x,y)s_{f,m}(z),$$
$$w(x,y,z) = 0 \tag{1}$$

The double subscript in shape function s (m for porous region, and f for fluid region) anticipates different velocity profiles within each region. The pressure then becomes function of x and y only. Considering the temperature also as function of x and y only (negligible variation in the z-direction),

$$p(x,y,z) = p(x,y), \qquad T(x,y,z) = T(x,y) \tag{2}$$

With Equations 1 and 2, the 3-D steady balance equations (Hsu and Cheng 1990) can be integrated in z, from zero to h. The resulting equations, valid for a slender cooling enclosure, are

$$\nabla \cdot \mathbf{V} = 0 \tag{3}$$

$$(\mathbf{V}\nabla)\cdot\mathbf{V} = \frac{\phi^2 h}{\int_0^h s_{f,m}^2\,dz}\left[-\frac{1}{\phi\rho}\nabla p' + J\nu\nabla^2\mathbf{V} + \left(\frac{2J}{h}\frac{ds_{f,m}}{dz}\bigg|_h - \frac{1}{K}\right)\nu\mathbf{V}\right] - \frac{c_F\phi^2}{K^{1/2}}|\mathbf{V}|\mathbf{V} \tag{4}$$

$$\mathbf{V}\cdot\nabla T = \frac{k_{f,m}}{\rho c_p}\nabla^2 T + \frac{1}{\rho c_p h}q'' \tag{5}$$

where $\mathbf{V}$ is the z-averaged fluid (seepage) velocity vector equal to $u\mathbf{i} + v\mathbf{j}$, p' is the pressure, and T is the temperature. Fluid quantities are the density ρ, specific heat c_p, thermal conductivity k_f, and kinematic viscosity ν. Saturated porous medium quantities are the effective thermal conductivity, k_m, porosity ϕ, effective viscosity coefficient J, permeability K, and Forchheimer inertia coefficient c_F. Other parameters of interest are the thickness h, depth d, and width t, of the enclosure (Figure 1, C and D).

The coefficient J shown in the Laplacian term of Equation 4 is the ratio between the effective (porous) kinematic viscosity (ν_m) and the fluid kinematic viscosity, $J = \nu_m/\nu$. For low permeability porous medium, this factor can be set equal to $1/\phi$ (Nield and Bejan 1992). Notice that when $\phi = 1$ and $K \to \infty$, Equation 4 takes the form of the Navier–Stokes equation, accurate for modeling flow through a nonporous region.

Once the shape functions for nonporous and porous regions are known, Equations 3–5 will form a system of two-dimensional (2-D) nonlinear partial differential equations. The dimensional simplification from three to two dimensions, although straightforward, requires the additional effort of determining the shape functions $s_{f,m}(z)$.

Within a nonporous region, the shape function is easily obtained from the fully developed velocity profile

$$s_f(z) = \frac{6z(h-z)}{h^2}, \quad \text{so}$$

$$\int_0^h s_f^2\,dz = \frac{6h}{5} \quad \text{and} \quad \frac{ds_f}{dz}\bigg|_h = \frac{-6}{h} \tag{6}$$

The situation is more complex when considering the flow within a porous medium region. Unfortunately, a unique closed form solution valid for all ranges of K and c_F does not exist, so it is necessary to proceed on a case-by-case basis. For low permeability matrices as considered here, low enough to validate a Brinkman-extended Darcy model (in a scaling form, $K \ll e^{3/2}\nu/(\phi u_{\text{in}} c_F)^{1/2}$), the fully developed velocity profile given by Kaviany (1985) leads to:

$$s_m(z) = \Gamma_1 - \Gamma_2\{e^{\beta[(z/h)-1]} + e^{-\beta(z/h)}\}$$

where

$$\Gamma_1 = \frac{(1 - e^{-2\beta})}{\left[1 - e^{-2\beta} - 2(1 - e^{-\beta})^2\beta^{-1}\right]},$$

$$\Gamma_2 = \frac{(1 - e^{-\beta})}{\left[1 - e^{-2\beta} - 2(1 - e^{-\beta})^2\beta^{-1}\right]}$$

and

$$\beta = (h^2\phi/K)^{1/2}$$

So,

$$\int_0^h s_m^2\, dz = h\Gamma_1 + h\Gamma_2^2\left[2e^{-\beta} - \frac{(1 - e^{-2\beta})}{\beta}\right] \quad \text{and}$$

$$\left.\frac{ds_m}{dz}\right|_h = \frac{\beta}{h}\Gamma_2(e^{-\beta} - 1) \tag{7}$$

The energy equation given by Equation 5 reveals the uniform volumetric heating model adopted here. This model is expected to be reasonably accurate when modeling heat transfer through thin enclosures. Notice that arrays designed by *TI* present identical top and bottom modules, in which case, the heat dissipated by the electronics is symmetric in z. The volumetric heat parameter of the rightmost term q''' represents the total power generated by the top and bottom electronic components per unit of volume, $q''' = (q''_t + q''_b)/h = q''/h$. This volumetric heat source is considered only within the region sandwiched by the two layers of electronic components (heating region), being zero everywhere else within the enclosure (the module housings are placed in contact with each other; therefore, the heating region is essentially a continuous region along the x-direction). Notice also that Equation 5 is valid for a nonporous region when k_f is used in the thermal diffusion term. Because secondary dispersion effects within the porous layer are not accounted for, the cooling effect obtained by solving the system of Equations 3–5 is conservative.

Boundary conditions are impermeable, nonslip, and adiabatic solid surfaces ($u = v = \partial T/\partial x = \partial T/\partial y = 0$), uniform and isothermal inlet coolant flow ($u = u_{\text{in}}$, $T = T_{\text{in}}$ and $v = 0$), and nondiffusion outlet boundary ($\partial u/\partial x = \partial T/\partial x = 0$).

The correctness of imposing nondiffusion temperature boundary condition at the outlet of the enclosure is now discussed. The zero diffusion outlet boundary condition was shown by Lage et al. (1991) to have negligible effect on the numerical simulation of ventilated 2-D enclosures. The same conclusion has been reached recently by Safi and Loc (1994) in their study of thermal stratification in a cavity with through flow. For Prandtl number larger than 1 (as used here), when convection predominates, the diffusive outlet boundary condition effect becomes less pronounced. The maximum temperature difference between results obtained with a nondiffusive outlet boundary and with a diffusive boundary at a constant temperature $T_{\text{out}} = T_{\text{in}}$, is less than 2%.

The solution of Equations 3–5 requires that the porosity, permeability, and inertia coefficient of the porous medium be known. These hydraulic parameters of compressed porous layers are obtained experimentally prior to the numerical simulations, as described in the next section.

Experimental procedure and results

An experimental setup is designed and built to obtain accurate determination of the flow (Darcy velocity) and intrinsic pressure drop across a porous layer inside a metallic block (Figure 2). The apparatus is used for obtaining the hydraulic characteristics (permeability and inertia coefficient) of nine porous layers, initially chosen based upon brazing surface and structural integrity, for building a microporous cold plate. Each porous layer is obtained by compressing a 1570 pores per meter aluminum 6101-O alloy matrix in the direction perpendicular to the flow direction (along H, Figure 2). The compression of the matrix is very advantageous as it enlarges the contact (interface) area between the porous layer and the solid surfaces of the cold plate. This, in turn, facilitates the brazing process and, in consequence, it improves the heat transfer across the interface and the structural rigidity of the cold plate.

The dimensions of the porous layers tested here conform with the cold-plate design for phased array radars. All aluminum blocks have inlet and outlet plena connected by a 76.2-mm long (L), 50.8-m wide (W), and 1.0-mm thick (H) test channel. A porous layer is placed inside the test channel, bonded to the surfaces, and covered with the top portion of the block. The bonding is carefully done to minimize possible adhesive intrusion through the pores of the layers. A block clear of porous layer (*clear* block) is also built for reference pressure drop measurements.

The air flow apparatus (Figure 2) includes a pressure regulator to adjust the maximum inlet air pressure (the inlet air line is linked to an external tank holding compressed air at 1.0 MPa). The air flow rate ranges from 1.7×10^{-6} to 7.2×10^{-5} m^3/s corresponding to a seepage velocity range of 0.033 to 1.436 m/s. Both rotameters (OMEGA FL111 and FL112) are calibrated to 2% of the reading value. The repeatability of both instruments is one-half percent of reading value.

The differential pressure is measured between the inlet and outlet ports of each block. A 300-Pa gauge micromanometer manufactured by Combustion Instruments Ltd. (0.1 Pa accurate) is utilized to measure the very small pressure drop. For the moderate pressure drop regime, a 0.5-kPa gauge inclined portable manometer, manufactured by Dwyer Inc., is used. The uncertainty of the instrument is 2.5 Pa. Two U-shaped manometers are used to measure the large pressure drop regime, a 46.5-kPa manometer, accurate to 30 Pa, and a 78.5-kPa manometer, accurate to 10 Pa.

It is important to point out that the pressure (speed) range used in the air test is small enough to neglect any compressibility effect. Therefore, the air density dependence on pressure, which can be approximately modeled by using the ideal gas law, is not accounted for here.

The inlet air temperature is recorded for correcting the air density and viscosity. A type J thermocouple wire is inserted in the air stream with the temperature displayed by a 450 AJT OMEGA thermocouple thermometer. The air properties are obtained by linear interpolation as a function of temperature (Air Properties Table, Bejan 1993). The outlet air temperature is also measured with a portable thermocouple thermometer. Air temperature difference between inlet and outlet is negligible (within thermocouple uncertainty of 0.5°C) in all experiments.

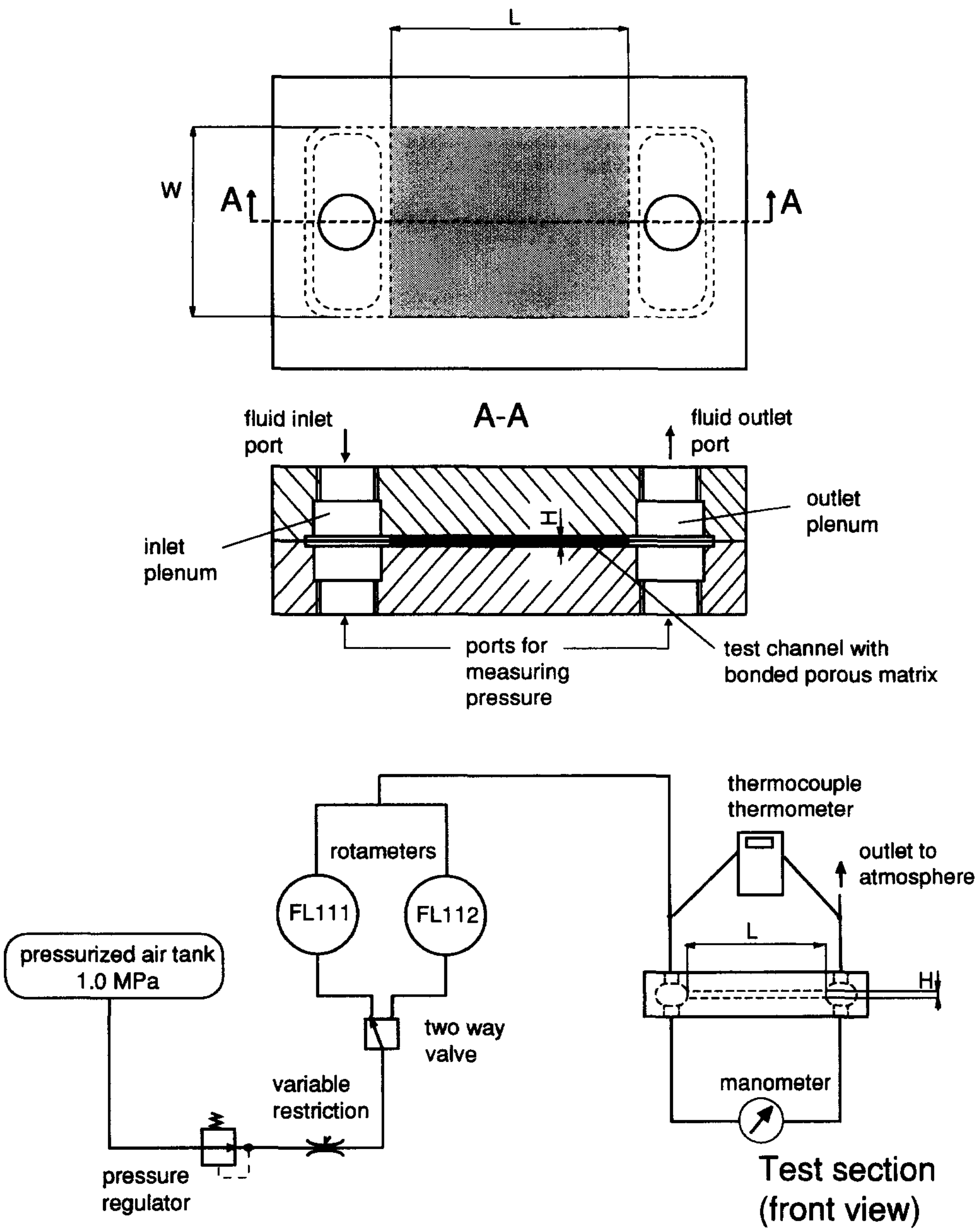

Figure 2 Block with aluminum porous matrix (top) and experimental setup for testing (bottom)

The test results represent the arithmetic average of at least five experimental runs for each block. The data acquisition starts at low flow rate, increasing in finite steps. No hysteresis is observed when acquiring data reducing the flow rate.

The compression ratio $r = H_u/H$ (where H_u is the initial—uncompressed—matrix thickness, and H is the final matrix thickness), of the layers varies form 4 to 14. Recall that all layers are compressed to a final thickness of one millimeter ($H = 1.0$ mm). The initial (uncompressed) volumetric porosity of the porous layer ϕ_u varies from 90 to 98%. The porosity of the compressed layers (Table 1) is obtained by calculating the solid volume an dividing it by the total volume of the matrix, $\phi = 1 - (V_s/V_m)$, where V_s is the solid phase volume, and V_m is the total volume of the porous layer (solid and fluid volumes). The solid (aluminum) volume of each porous layer is calculated by weighing each porous sample after compression and dividing it by the aluminum alloy density (2681.4 kg/m^3). The total volume is measured directly.

From the experimental measurements, a Darcy velocity is computed for each pressure drop by dividing the volumetric flow rate $\dot{Q}$ by the cross-section area of the test channel S ($= WH$):

$$v_D = \frac{\dot{Q}}{S} \tag{8}$$

The pressure differential, produced by the porous layer only, is computed by subtracting the pressure drop of the clear (no porous insert) block Δp_f from the pressure drop of the porous block Δp_m at each velocity

$$\Delta p(v_D) = \Delta p_m(v_D) - \Delta p_f(v_D) \tag{9}$$

Table 1 Uncompressed porosity ϕ_u, compression ratio r, porosity ϕ, permeability K, Forchheimer coefficient c_F, and uncertainties (U_K, U_{c_F}) of mechanically compressed aluminum matrices

Layer no.	ϕ_u, %	r	ϕ, %	K, 10^{-10} m^2	U_K, %	c_F	U_{c_F}, %
1	96	7	**64**	**11.4**	5.4	**0.37**	8.0
2	96	9	**62**	**5.9**	4.7	0.40	8.8
3	96	11	56	3.7	4.5	0.45	9.2
4	96	14	47	**1.8**	3.6	0.41	11.5
5	94	7	56	6.1	5.2	0.47	8.2
6	94	9	46	3.2	4.7	0.53	8.8
7	92	5	60	9.2	5.2	0.38	8.2
8	92	7	**31**	**5.4**	4.7	0.42	8.8
9	90	5	43	2.7	5.8	**0.84**	7.9

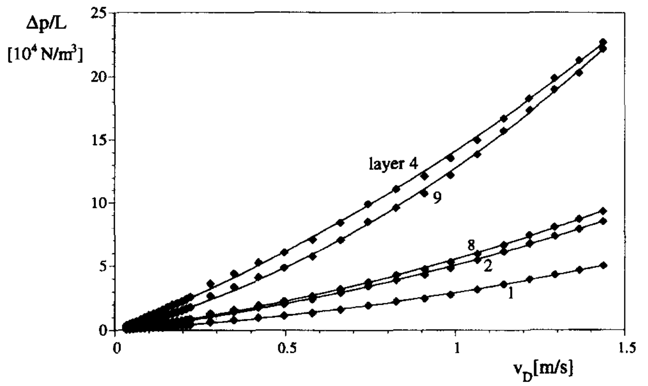

Figure 3 Intrinsic pressure gradient versus seepage velocity: experimental results for air

Equation 9 isolates the pressure drop effect of the porous layer from the pressure drop caused by the inlet and outlet connections, plena, and channel surfaces. For the pairs $(v_D, \Delta p/L)$ a quadratic interpolation following

$$\frac{\Delta p}{L} = \frac{\mu}{K} v_D + \frac{\rho c_F}{K^{1/2}} v_D^2 \tag{10}$$

is performed, using the least-square method. The permeability and Forchheimer coefficients for each specific porous layer are obtained directly from the quadratic interpolation. This procedure is shown (Antohe et al. 1996) to be consistent with the experimental range utilized and to yield more precise coefficient values, because the method does not rely on extrapolation or on visual estimation of an asymptotic value.

Table 1 summarizes the hydraulic results obtained for the nine layers tested. The uncertainty values for the permeability and Forchheimer coefficients are calculated following the methodologies presented in detail in Antohe et al. (1996). These experimentally obtained values are used in the mathematical model presented in the previous section for the numerical simulation of the cold plates.

Figure 3 presents a sample of the experimental pressure drop *versus* velocity across layers 1, 2, 4, 8, and 9. An important observation from Figure 3 is that, indeed, the flow through these mechanically compressed microporous layers behave as flow through a porous medium, that is, the intrinsic pressure gradient is quadratic in seepage velocity.

From the experimental hydraulic data of Table 1, five layers were chosen for the numerical simulations. These layers represent extreme cases, as highlighted in Table 1, of: maximum porosity and permeability and minimum inertia coefficient—layer 1; minimum permeability—layer 4; minimum porosity—layer 8; maximum inertia coefficient—layer 9. Also included is layer 2, which presents almost the same permeability and twice the porosity of layer 8. (These are represented in Table 1 by **boldface** type.)

One concern of using air flow for the hydraulic experimental testing of the porous layers is the possibility of achieving Knudsen regime at the low end of the velocity spectrum. As Kaviany (1991) mentioned, at low pressure and small pore size (which is related with permeability), a velocity slip can occur as the mean path of the gas molecules approaches the pore dimension. This "slippage" effect reveals itself by means of an increase in the flow rate as the pressure gradient is decreased, fact that leads to an apparently higher permeability.

The Knudsen number is defined as:

$$\mathrm{Kn} = \frac{\lambda}{C} \tag{11}$$

with the mean path of gas molecules λ computed from

$$\lambda = \frac{k_B T}{2^{2.5} \pi R_m^2 p} \tag{12}$$

where the constant k_B is 1.381×10^{-23} J/K, and the radius of collision cross section for air is $R_m = 1.805 \times 10^{-10}$ m. The pore dimension C is estimated from the Karman–Kozeny equation:

$$C \sim (1 - \phi)\left(\frac{150K}{\phi^3}\right)^{0.5} \tag{13}$$

A maximum Knudsen number $\mathrm{Kn}_{\max}$ for each layer is computed from Equation 11 using K from Table 1 and the minimum pressure of each experiment. All $\mathrm{Kn}_{\max}$ values are smaller than 1; therefore, the Knudsen regime is avoided in all tests.

Numerical simulations

A cold plate for a phased-array radar system considered by *TI* consists of an enclosure measuring 0.5 m (width t) by 0.15 m (depth d) by 0.001 m (thickness h). Inlet and outlet ports measure 0.025 m (e) in depth (see Figure 1 C). The electronic modules are approximately 0.075 m deep, same as the heating region d_h centered in the y-direction.

The mechanically compressed porous layer, also centered in the y-direction, occupies a region that extends beyond the heating region being 0.1-m deep (see Figure 1C), aligned with the inlet and outlet ports. The ϕ, K, and c_F properties of the layer, obtained experimentally, are from Table 1. The thermal conductivity of the layer (6061-T0 aluminum alloy) is $k_s = 216$ W/mK.

Typical inlet coolant temperature is 20°C, and the total heat flux dissipated by the electronics is 18.2 kW/m^2. The coolant is polyalphaolefin (PAO—a synthetic oil used for cooling military avionics) with density, kinematic viscosity, thermal conductivity, and specific heat equal to, respectively: 790 kg/m^3, 7.9×10^{-6} m^2/s, 0.143 W/mK, and 2 kJ/kgK (from Chevron 1981). The mass flow rate of PAO varies from 6×10^{-3} to 37×10^{-3} kg/s, equivalent to inlet velocity from 0.3 m/s to 1.9 m/s.

The effective thermal conductivity k_m of each compressed porous layer is estimated using the phase-symmetry model recently proposed by Hsu et al. (1994): layer $1 = 29$ W/mK; layer $2 = 30$ W/mK; layer $4 = 50$ W/mK; layer $8 = 93$ W/mK; layer $9 = 63$ W/mK. Notice that the porous modified thermal conductivity is much higher than the fluid thermal conductivity ($k_{\text{PAO}} = 0.143$ W/mK), therefore, it is the latter that effectively controls the thermal diffusion process within the enclosure.

The balance Equations 3–5, with shape parameters listed in Equations 6 and 7, are solved using the finite volume method with SIMPLE algorithm (Patankar 1980) and QUICK scheme (Leonard 1979). Discretized equations are solved with the efficient tri-diagonal-matrix algorithm using an implicit alternating-direction Gauss–Seidel iterative method. The present code is a modified version (upgraded) of the one validated against experimental results by Lage et al. (1991) simulating indoor pollutant transport through a ventilated enclosure.

Convergence criteria are: relative norm of pressure gradient being smaller than 10^{-6} for flow convergence, and relative norm of volume averaged temperature being smaller than 10^{-5} for energy equation convergence. After performing extensive grid accuracy tests, it is observed that a nonuniform (with grid lines clustered near solid interfaces and near nonporous–porous interfaces) 110×70 grid is sufficient to guarantee a 3% or smaller discrepancy with results obtained with a 160×100 grid.

The accuracy of the numerical simulations is also checked by performing a global energy balance within the enclosure. It is easy to show that for convection dominated heat transfer, the averaged outlet fluid temperature has to satisfy

$$\overline{T}_{\text{out}} = T_{\text{in}} + \frac{q''}{\rho c_p u_{\text{in}}} \frac{t d_h}{e h} \tag{14}$$

where d_h is the depth of the heating section. All results satisfy this global balance within 0.01%.

The separation of variables invoked in Equation 1, as, for example, $v(x, y, z) = v(x, y)s(z)$, when the flow region is a sequence of nonporous–porous–nonporous regions assumes that all hydrodynamic development lengths are negligibly small. For transition from nonporous to porous region, the assumption is accurate as long as the Darcy number is small: the developing length in a low permeability porous region is predicted as $x_m \sim (h/e)K^{1/2}$ (Nield and Bejan 1992), in the present case, $x_m \sim 10^{-6}$ m, shorter than the porous layer depth of 0.1 m.

The transition from porous to nonporous region is more subtle. For nonporous flow through parallel plates, with uniform incoming flow, the entrance length is predicted as $x_f = 0.0065 h^2 u_{\text{in}}/\nu$ (Sparrow 1955). So, the maximum developing length is less than 0.0025 m, which is about 10 times smaller than the shortest plenum depth assumed here equal to 0.025 m. Because the flow coming out of a low permeability porous region is not uniform (distorted due to Brinkman effect) the development length is expected to be even shorter (this effect might be negligible if porosity variation near the surface is included in the analysis).

A note is necessary regarding the thermal equilibrium assumption invoked by the mathematical model in Equation 5. This assumption is known to deteriorate for high Reynolds number and high Darcy number, depending on the solid matrix-to-fluid thermal diffusivity ratio. This dependence is not a simple one, as indicated in the work of Amiri and Vafai (1994) considering a porous medium made of identical spherical particles, particle Reynolds number from 0 to 450, and Darcy number from 0 to 15×10^{-7} (see their Figure 7). The solid matrix and fluids considered here present diffusivity ratio around 1500. The particle-based Re is less than 150, and the Darcy number (based on inlet depth) is approximately 10^{-6}. Although Amiri and Vafai's qualitative mapping does not go beyond diffusivity ratio 25, it anticipates the thermal equilibrium assumption to be a reasonable approximation.

Finally, a reviewer questioned the validity of using the derived volume-averaged Equations 3–5 in a system with large aspect ratios as the one considered here. We believe the model is valid as long as the representative pore dimension of compressed layers is much smaller than the layer thickness (smaller macroscopic dimension), as verified in all present cases.

Numerical results

In Figure 4 the equivalent pressure gradient from inlet port to outlet port is presented as function of PAO inlet fluid speed. The equivalent permeability and inertia coefficient values of each configuration (porous layer) are obtained from least square curve fitting using Equation 10. The results are included in the figure. The pressure gradient curves indicate a predominance of Darcy effect as expected because of the flow rates, the closeness of the plates (small h—notice in Equation 4 that the viscous effect of top and bottom plates is represented by a Darcy-like term) and the relatively low permeability of the porous layers. In fact, Lage et al. (1996) derived an expression for comparing the viscous effect of the plates with the viscous effect of the porous layer. In

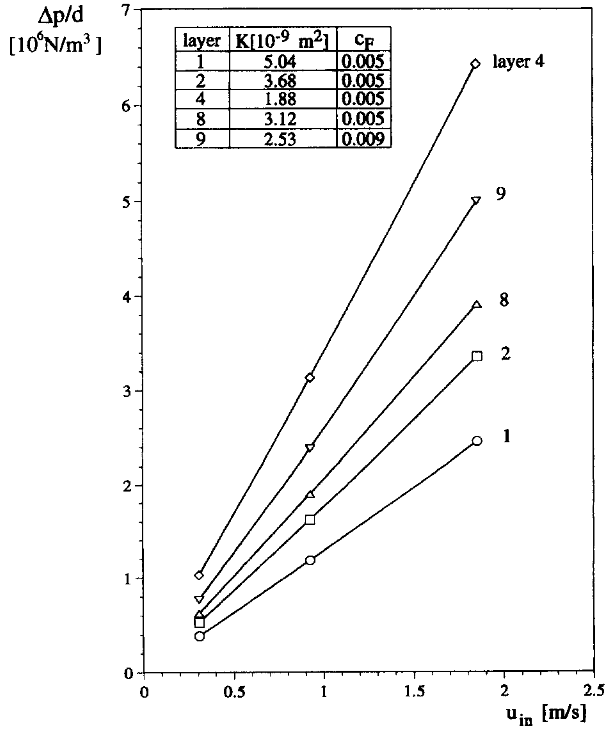

Figure 4 Equivalent intrinsic pressure gradient across the cold plate versus inlet velocity of PAO: numerical results

dimensional form, when $K \ll (\phi h^2)/(-2f_m)$, then the Darcy drag effect predominates. This condition is satisfied for all cases shown in Figure 4 by one order of magnitude. The inertia coefficient has little effect on the pressure drop (the maximum equivalent permeability-based Reynolds number $u_{in}eK^{1/2}/(\nu t)$ is equal to 0.89).

The maximum pressure gradient from Figure 4 is attained with the lowest permeability porous layer, layer 4, the least efficient configuration in hydraulic terms. The lowest pressure gradient is attained with layer 1 that presents the highest permeability.

Figure 5 presents the thermal and hydraulic results of porous layers 1, 2, 4, 8, and 9. Three graphs are combined, all of them shown in terms of the coolant mass flow rate, $\dot{m}$. In the top section of the figure, the system total pressure drop (from inlet to outlet) is presented. The middle graph displays the maximum temperature difference along the x-direction of Figure 1 within the heating region (electronics region) of the cold plate. The bottom graph depicts the maximum temperature within the porous region.

This ensemble of results is of engineering value as a design tool following three simple steps: (1) choose a porous layer; (2) determine the maximum flow rate of coolant $\dot{m}_{max}$ from the intercept of an extended horizontal line from the maxium pressure drop available for the particular system Δp_{sys} and the curve of the selected layer in the top graph; (3) obtain the minimum flow rate $\dot{m}_{min}$ by extending an horizontal line from the maximum allowed temperature difference value $(\Delta T_{max})_{sys}$ for the system to the curve of the selected layer (middle graph). Once setting the desired coolant flow rate, within the acceptable flow rate domain $(\dot{m}_{min} \leq \dot{m} \leq \dot{m}_{max})$, the maximum temperature within the porous region of the enclosure is obtained directly from the ordinate of the bottom graph.

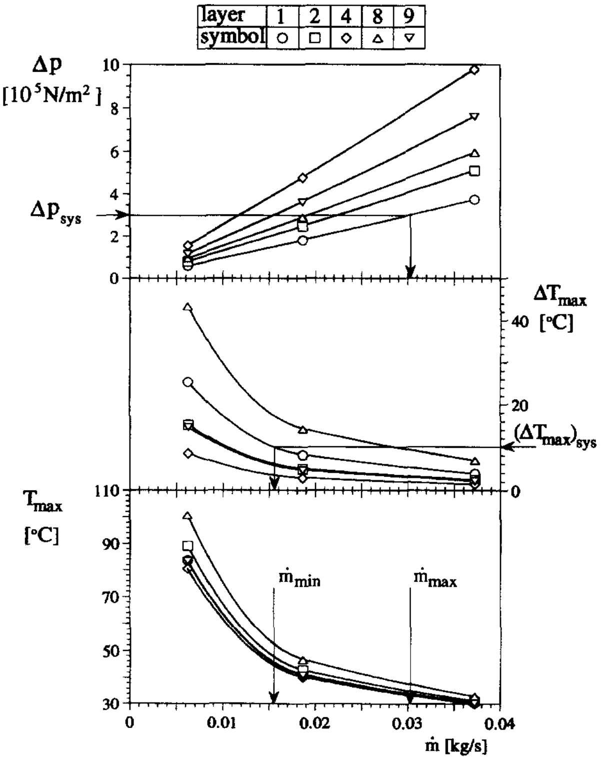

Figure 5 Pressure drop Δp, maximum temperature difference along x-direction (ΔT_{max}), maximum temperature within porous layer (T_{max}), *versus* mass flow rate of PAO: numerical results

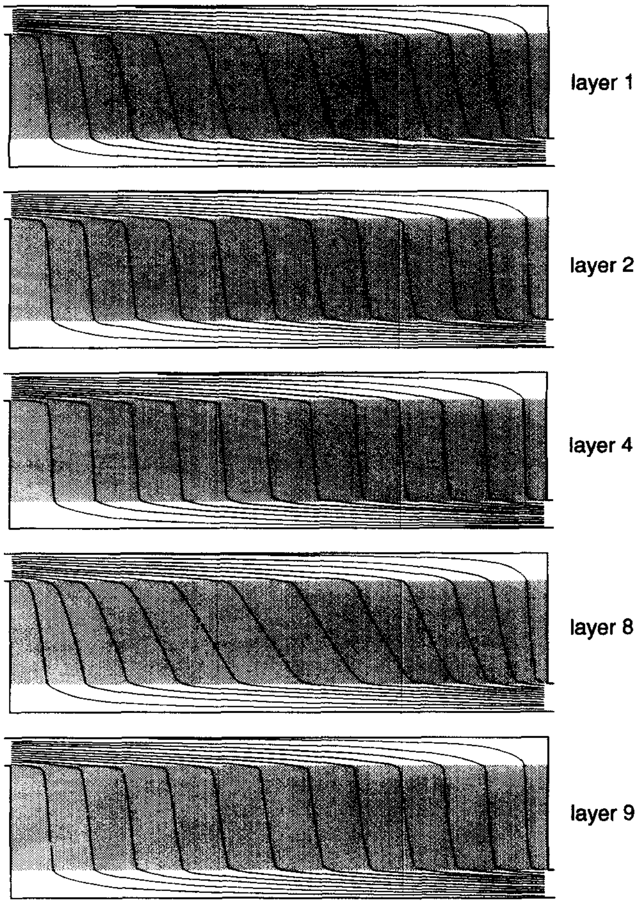

Figure 6 Equally spaced streamlines for different porous layers (shaded area indicates location of porous layer)

The maximum temperature and the maximum temperature difference, along the x-direction (middle and bottom graphs), curves indicate that a system with layers 2 and 9 behave similarly, although having different effective thermal conductivity values. This might be an indication that the heat transport is predominantly by convection. A system with porous layer 4 is the most efficient from a thermal point of view, because it yields the lowest maximum temperature and temperature difference among all layers. The worst system would be with layer 8. In any event, the worst scenario points to a maximum pressure drop of less than 10^6 Pa and a maximum ΔT_{max} of less than 45°C.

Figures 6 and 7 present, respectively, the streamline and isotherm distributions for each layer, with mass flow rate of PAO equal to 6.2×10^{-3} kg/s. The shaded area indicates the region occupied by the porous layer. The heating region (Figure 7) is delimited by dashed lines.

All streamline distributions indicate the strong effect of the porous layer in distributing the coolant flow. Recall that the objective is to have streamlines as vertical as possible within the heating region of the cold plate. It is clear that porous layer 4 achieves the most uniform flow distribution and, consequently, more uniform temperature within the heating region, confirming the previous observations of best thermal performance with highest hydraulic head loss.

An interesting result is the streamline distribution of the system with layers 2 and 8. Notice, from Table 1, that layer 2 has

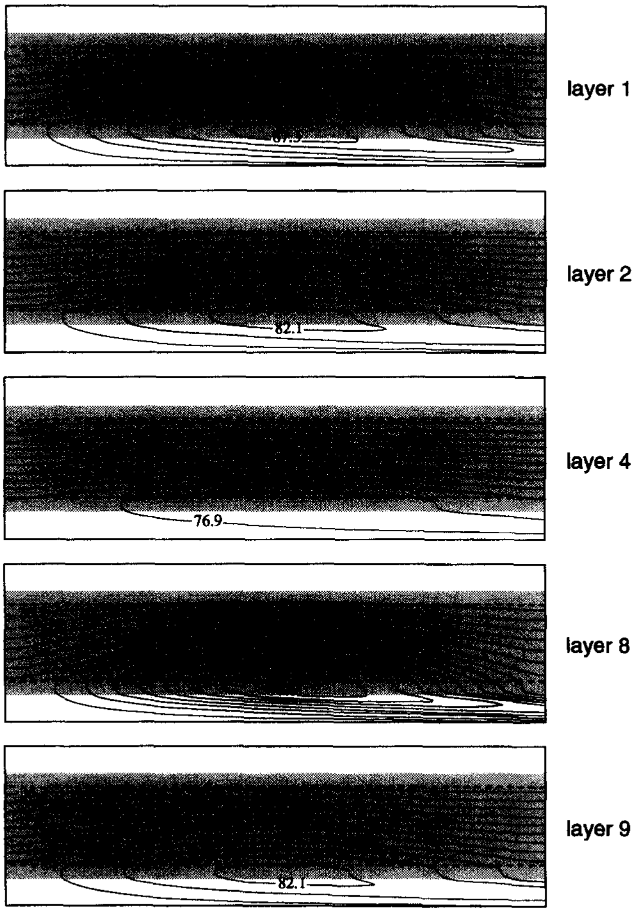

Figure 7 Isotherm distribution of PAO for the same porous layers as in Figure 6 (heating section delimited by dashed lines)

twice the porosity of layer 8 and almost the same permeability. However, layer 8 behaves as having larger permeability (see how streamlines of layer 2 are more vertical than those of layer 8). Equation 4 indicates that increasing the porosity of a porous layer, maintaining the same permeability, is equivalent to maintaining the porosity the same and decreasing its permeability. This explains the streamline behavior.

The isotherms present a stratified temperature distribution within most of the heating region, as desired. The maximum temperature is located outside the heating region, within the porous layer. The flow distortion seen in Figure 6, particularly for layers 8 and 1, translates into a less uniform temperature, with better cooling near the side walls. Figures 6 and 7 support a convection-dominated heat transfer mode assumption. In fact, calculating the equivalent Peclet number of the system, the minimum value is around 6.

Closure

Mechanically compressed aluminum matrices are considered in the design of heat exchangers for cooling high-power microelectronics systems. Nine matrices manufactured in aluminum alloy at various densities and void sizes are fully tested, using air, for hydraulic characterization in terms of porosity, permeability, and inertia coefficient. The assumed porous medium behavior of these matrices is confirmed experimentally. The parameter values vary as: $0.3 < \phi < 0.7$, 1.8×10^{-10} m$^2 < K < 1.2 \times 10^{-9}$ m^2, and $0.3 < c_F < 0.9$. These parameters, fundamental for the design and optimization of the microporous heat exchangers, are input data for several numerical simulations of a real system. Results indicate that the hydraulic efficiency of the system, in terms of pressure drop, can vary by five times depending on the characteristics of the porous layer used in the heat exchanger. The thermal efficiency of the microporous heat exchanger in terms of maximum temperature in the system as well as in terms of maximum temperature variation transversal to the main coolant flow direction is also presented. Minimization of this temperature variation is an essential requirement for improving the reliability of high-power electronics telecommunication systems. The results indicate that the microporous cold-plate design is capable of yielding maximum transversal temperature difference of 2°C, using PAO as coolant, with a pressure drop across the porous layer of less than 10^6 Pa for a mass flow rate from 0.018 kg/s to 0.038 kg/s. In this case, the maximum temperature within the cold plate is less than 20°C above inlet coolant temperature.

Acknowledgments

The continuous financial and technical support provided by Texas Instruments Incorporated during this project is greatly appreciated.

References

Amiri, A. and Vafai, K. 1994. Analysis of dispersion effects and non-thermal equilibrium non-Darcian, variable porosity incompressible flow through porous medium. *Int. J. Heat Mass Transfer*, **37**, 939–954.

Antohe, B. V., Lage, J. L., Price, C. D. and Weber, R. M. 1996. Experimental determination of permeability and inertia coefficients of mechanically compressed aluminum porous matrices. *J. Fluids Eng.*, in press

Bejan, A. 1993. *Heat Transfer*. Wiley, New York, 646

Bergles, A. E. 1985. Techniques to augment heat transfer. *Handbook of Heat Transfer Applications*, W. M. Rohsenow et al. (eds.), McGraw-Hill, New York

Chevron, 1981. *Synfluid Synthetic Fluids*. Physical Property Data

Hsu, C. T. and Cheng, P. 1990. Thermal dispersion in a porous medium. *Int. J. Heat Mass Transfer*, **33**, 1587–1597

Hsu, C. T., Cheng, P. and Wong, K. W. 1994. Modified Zehner–Schlunder models for stagnant thermal conductivity of porous media. *Int. J. Heat Mass Transfer*, **37**, 2751–2759

Kaviany, M. 1985. Laminar flow through a porous channel bounded by isothermal parallel plates. *Int. J. Heat Mass Transfer*, **28**, 851–858

Kaviany, M. 1991. *Principles of Heat Transfer in Porous Media*. Springer-Verlag, New York

Kuzay, T. M., Collins, J. T., Khounsary, A. M. and Morales, G. 1991. Enhanced heat transfer with metal-wool-filled tubes. *Proc. ASME/JSME Thermal Engineering Joint Conference*, **5**, 451–459

Lage, J. L., Bejan, A. and Anderson, R. 1991. Efficiency of transient contaminant removal from a slot ventilated enclosure. *Int. J. Heat Mass Transfer*, **34**, 2603–2615

Lage, J. L., Weinert, A. K., Price, C. D. and Weber, R. M. 1996. Numerical study of a low permeability microporous heat sink for cooling phased-array radar systems. *Int. J. Heat Mass Transfer*, **39**, 3633–3647

Leonard, B. P., 1979. A stable and accurate convective modeling procedure based on quadratic upstream interpolation. *Comput. Meth. Appl. Mech. Eng.*, **19**, 59–98

Lindemuth, J. E., Johnson, D. M. and Rosenfeld, J. H. 1994. Evaluation of porous metal heat exchangers for high heat flux applications. In *Heat Transfer in High Heat Flux Systems*, A. M. Khonsary, T. W. Simon, R. D. Boyd and A. J. Ghajar (eds.), HTD, vol. **301**, ASME, New York, 93–98

Nield, D. A. and Bejan, A. 1992. *Convection in Porous Media*. Springer-Verlag, New York

Patankar, S. V. 1980. *Numerical Heat Transfer and Fluid Flow*, Hemisphere, Bristol, PA

Peng, X. F., Wang, B. X., Peterson, G. P. and Ma, H. B. 1995. Experimental investigation of heat transfer in flat plates with rectangular microchannels. *Int. J. Heat Mas Transfer*, **38**, 127–137

Safi, M. J. and Loc, T. P. 1994. Development of thermal stratification in a two-dimensional cavity: A numerical study. *Int. J. Heat Mass Transfer*, **37**, 2017–2024

Sparrow, E. M. 1955. Analysis of laminar forced convection heat transfer in the entrance region of flat rectangular ducts. *NACA* **TN-3331**

Walpole, J. N. and Missaggia, L. J. 1993. Microchannel heat sinks for two-dimensional diode laser array. *Surface Emitting Semiconductor Lasers And Arrays*, 1st ed., G. A. Evans and J. M. Hammer (eds.), Academic Press, New York